HOKKAIDO UNIVERSITY

| | |
|---|---|
| Title | Synthesis of ZrN-SiO2 core-shell particles by a sol-gel process and use as particle‐based structured coloring material |
| Author(s) | Noguchi, Shinji; Miura, Akira; Tadanaga, Kiyoharu |
| Citation | Journal of the American Ceramic Society, 107(10), 6885-6895<br>https://doi.org/10.1111/jace.19981 |
| Issue Date | 2024-07 |
| Doc URL | https://hdl.handle.net/2115/100469 |
| Rights | This is the peer reviewed version of the following article:Noguchi S, Miura A, Tadanaga K. Synthesis of ZrN-SiO2 core-shell particles by a sol-gel process and use as particle-based structured coloring material. J Am Ceram Soc. 2024; 107: 6885-6895. https://doi.org/10.1111/jace.19981, which has been published in final form at https://doi.org/10.1111/jace.19981. This article may be used for non-commercial purposes in accordance with Wiley Terms and Conditions for Use of Self-Archived Versions. This article may not be enhanced, enriched or otherwise transformed into a derivative work, without express permission from Wiley or by statutory rights under applicable legislation. Copyright notices must not be removed, obscured or modified. The article must be linked to Wiley’s version of record on Wiley Online Library and any embedding, framing or otherwise making available the article or pages thereof by third parties from platforms, services and websites other than Wiley Online Library must be prohibited. |
| Type | journal article |
| File Information | ShinjiNoguchi2024_JAmCeramSoc_107-10_6885-6895.pdf |

Hokkaido University Collection of Scholarly and Academic Papers : HUSCAP

# Synthesis of ZrN–$SiO_2$ Core–shell Particles by a Sol-gel Process and Use as Particle-based Structured Coloring Material

*Shinji Noguchi,[1] Akira Miura,[2] Kiyoharu Tadanaga[2*]*

[1]Graduate School of Chemical Sciences and Engineering, Hokkaido University, Kita-13, Nishi-8, Kita-ku, Sapporo 060-8628, Japan

[2]Faculty of Engineering, Hokkaido University, Kita-13, Nishi-8, Kita-ku, Sapporo, 060-8628, Japan

**KEYWORDS:** core-shell particle, sol-gel process, metal nitride, plasmonics, structural color

**ABSTRACT:** ZrN–$SiO_2$ core–shell particles were prepared, where the ZrN core nanoparticles and $SiO_2$ shell were designed to exhibit localized surface plasmon resonances (LSPRs) and structural coloring. The heating of $ZrO_2$ nanoparticles with $Mg_3N_2$ under a nitrogen gas flow produced ZrN nanoparticles with a diameter in the range of 10–20 nm. The dispersion of ZrN nanoparticles in water exhibited an absorption maximum at approximately 700 nm owing to LSPRs. An $SiO_2$ shell was formed on the ZrN nanoparticles using a sol-gel process. Scanning transmission electron microscopy confirmed the formation of ZrN–$SiO_2$ core–shell particles containing ZrN particles with a diameter of approximately 10 nm. The $SiO_2$ shell thickness was controlled by varying the reaction time to form $SiO_2$. The use of particles as a structural component of a structural color material owing to the high uniformity of the size of obtained core-shell particles was investigated. The obtained ZrN–$SiO_2$ core–shell particles were arrayed on a glass substrate using a layer-by-layer method. The particle-stacked film of the ZrN–$SiO_2$ core–shell particles exhibited the maximum reflection depending on the particle size of the $SiO_2$ shell.

## Introduction

Core-shell particles feature a central core containing a distinct component enveloped by an outer shell composed of another compound. Core-shell particles present a method for preparing materials with novel properties and applications ranging from catalysis[1–6] to electronic,[7, 8] magnetic,[9, 10] or optical devices.[11–13] In inorganic compounds, a conspicuous emphasis is on the functionality of core-shell particles comprising metal nitrides. Core-shell particles containing metal nitrides have unique characteristics that hold the potential for a diverse range of applications, including catalysis,[14, 15] optical sensing,[16] and energy conversion.[17] In recent years, several core-shell nanostructures composed of metal nitrides and metal oxides have been prepared, and their functions have been reported.[18–21] In the combination of metal nitrides and oxides, the preparation of core-shell particles requires a component encompassing the selection of materials, choice of the synthesis process, and envisaging of desired properties. The core-shell architecture confers upon these particles an amalgamation arising from the unique traits of metal nitrides and oxides. By careful selection of the core and shell constituents and designing structures from the chemical and physical perspectives, such as catalytic activity, magnetism, stability, and surface area, a variety of properties that surpass those of homogeneous materials or simple mixtures can be achieved. For example, cobalt-based nitride-core oxide shells,[18] $Fe_2N$ stabilized by core-shell formation with iridium oxide,[15] and $Fe_4N$–$IrO_2$ core–shell particles[19] have successfully acted as catalysts while enhancing both the catalytic activity and stability. The advantages arising from the combination of metal oxides and nitrides have been reported in the field of energy materials.[20] Core–shell nanostructures of metal nitrides and metal oxides have also been explored in magnetic nanodevices and biomedical applications.[21] Thus, the core-shell formation of metal oxides and metal nitrides has the potential to adjust the interactions between metal oxide and metal nitride, increase stability, and rise new materials. However, metal nitride/metal oxide core–shell materials have not been employed in applications to exploit both the optical properties of the metal nitride core and the morphology of the entire core-shell particle.

This study considers ZrN as a core material because it exhibits localized surface plasmon resonances (LSPRs). Moreover, LSPR is a phenomenon characterized by the resonance of electrons on the surface of a particle, induced by collective vibrations. The selective absorption of particular light wavelengths by materials is attributed to electron resonance upon light absorption, resulting in collective vibrations. LSPR occurs in noble metal nanoparticles, such as gold, silver, and platinum. Recently, it was reported that metal nitride nanoparticles exhibited LSPRs. Karaballi et al. reported that TiN, ZrN, and HfN nanoparticles, which are nitrides of group four elements, exhibited LSPR.[22] Exarhos et al. synthesized core–shell zirconium nitride–silicon oxynitride nanoparticles using chemical vapor deposition (CVD) and confirmed that the formed nanoparticles exhibited LSPR.[23] The absorption wavelength was controlled by coating the ZrN nanoparticles with silicon oxynitride. Moreover, ZrN–$SiO_2$ core-shell particles were theoretically suggested to boost the efficiency of Pb-free perovskite solar cells to reach up to 20%.[24] From an optical perspective, ZrN and core-shell nanoparticles containing ZrN are expected to gain attention in the future. However, a process for preparing ZrN–$SiO_2$, which is ZrN coated with $SiO_2$, has not yet been reported. The formation of ZrN–$SiO_2$ core–shell particles at ambient temperature and pressure is more valuable than the formation of these particles using processes such as plasma CVD or nitridation with $NH_3$ gas. Some studies discussed the synthesis of metal nitrides without the use of $NH_3$ gas.[25, 26] In particular, the liquid-phase process is appropriate as a low-energy process for preparing ZrN–$SiO_2$ core–shell particles in mass production.

We utilized the Stöber process,[27] as a liquid-phase process, to prepare core-shell particles. The Stöber process is a typical method for synthesizing monodisperse silica particles.[28] The Stöber process involves hydrolysis and polycondensation of silicon alkoxides under basic conditions to obtain uniformly sized particles. Thus, the Stöber process has been used for the core-shelling of Au,[29–34] Ag,[35] $Fe_2O_3$,[36] $Fe_3O_4$,[37] $CsPbBr_3$,[38] CdSe/$Cd_xZn_{1-x}S$,[39] and nanoscale diamond[40] with silica.

In this study, ZrN nanoparticles exhibiting LSPR were synthesized, and ZrN–$SiO_2$ core-shell particles were prepared by coating silica around the obtained ZrN nanoparticles using the sol-gel method. By

employing these particles as a material that constitutes the structural color, we evaluated the possibility of achieving a material that reflects specific wavelengths from a highly uniform particle size.

## RESULTS AND DISCUSSION

The mixture of $ZrO_2$ nanopowder (Figure S1) and $Mg_3N_2$ powder was heated at 1000 °C to obtain dark green products. The products obtained after the reaction contained ZrN, MgO, and $Mg_3N_2$ (Figure S2). ZrN and MgO were formed through the reaction of $ZrO_2$ with $Mg_3N_2$, while the residual $Mg_3N_2$ was due to an excess of 3 molar equivalents of $Mg_3N_2$ added to $ZrO_2$, resulting in unreacted $Mg_3N_2$ remaining. The reaction of $ZrO_2$ and $Mg_3N_2$ forming ZrN is as follows.[22]

$$6\,ZrO_2 + 4\,Mg_3N_2 \rightarrow 6\,ZrN + 12\,MgO + N_2$$

The obtained dispersion, which was washed in the HCl solution, was blue in color, as shown in **Figure 1(a)**. The products were observed by transmission electron microscopy (TEM) to confirm their morphology. **Figure 1(b-d)** shows the TEM image of the products. The products consisted of particles, and each particle size was in the range of 10–20 nm. From **Figure 1(d)**, it can be observed that the interplanar spacing in the particles is 0.28 nm. This spacing corresponds to the (100) plane of ZrN. **Figure 1(e)** shows the X-ray diffraction (XRD) profile of the dried particles. The XRD profile of the products exhibits peaks originating from the ZrN phase. The result indicates that the washing process dissolved and removed the unreacted $Mg_3N_2$ and the formed MgO, while the insoluble ZrN remained. Peaks observed at 33° and 45° in the XRD pattern are considered to be attributable to impurities that formed during the washing process. The particle size distribution was derived by analyzing the small-angle X-ray scattering (SAXS) intensity (Figure S3). The particle size distribution shows a mode at approximately 3 nm, which decreases as the particle size increases, as shown in **Figure 1(f)**. The average particle size is approximately 12 nm. The average crystal size of the obtained ZrN, derived from the XRD profile using

the Debye–Scherrer equation, is 11 nm. This result satisfactorily agrees with the average particle size of ZrN determined from SAXS measurements (12 nm), suggesting the validity of the particle size distribution calculated using the SAXS. These particles were sufficiently small to exhibit LSPRs.[22] The absorption spectrum of the ZrN nanoparticle dispersion exhibits a peak at approximately 700 nm, as shown in **Figure 1(g)**. The dispersion of ZrN nanoparticles exhibited increased absorbance at wavelengths below 400 nm. This phenomenon is attributed to Rayleigh scattering by ZrN particles. Rayleigh scattering is applicable when particle size $d$ is considerably smaller than the wavelength of light $\lambda$, typically represented as $d<<\lambda$. This implies significant Rayleigh scattering occurs when the particle diameter is less than one-tenth of the wavelength, i.e., $d < \lambda/10$.[41] Given the average particle size of ZrN nanoparticles was 12 nm, it was posited that light with wavelengths shorter than 400 nm is strongly scattered, resulting in reduced transmitted light intensity.

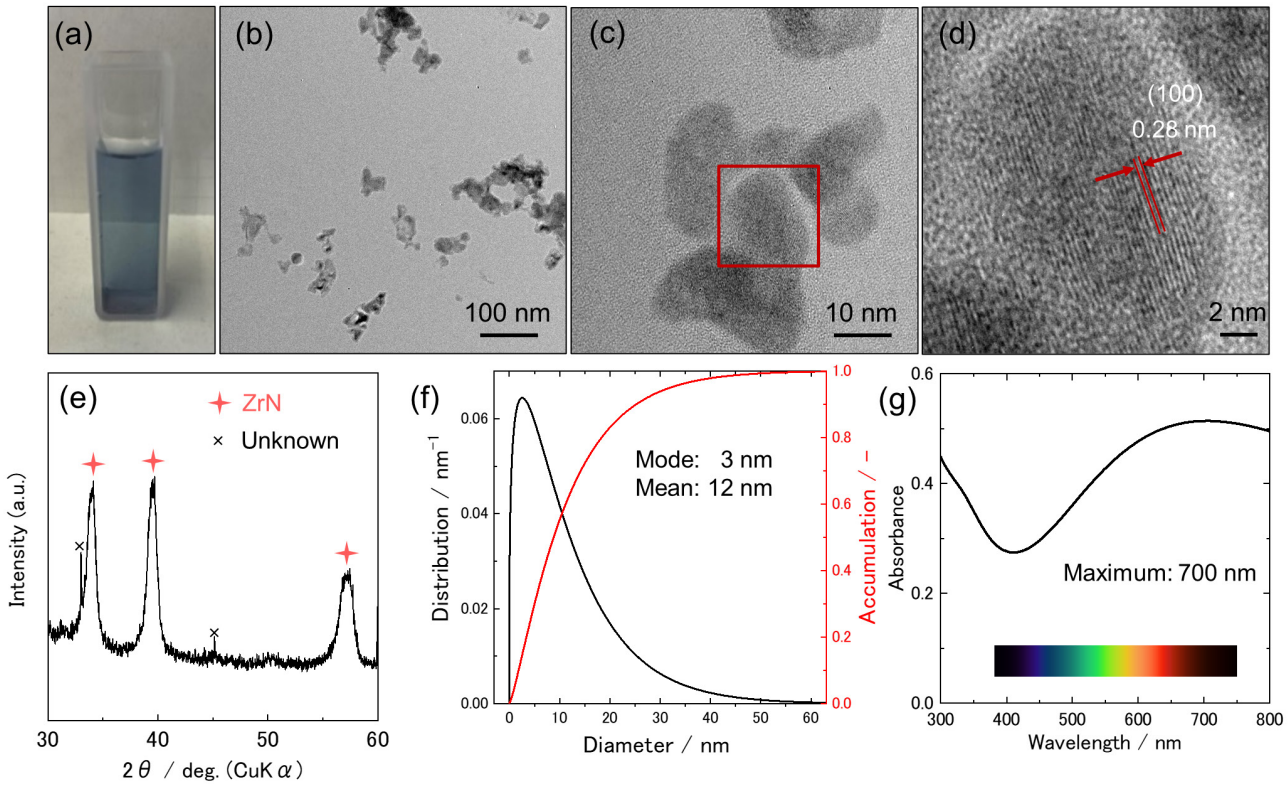


**Figure 1.** (a) Photograph of the diluted particle dispersion. TEM images of the product from $ZrO_2$ and $Mg_3N_2$.; (b) low magnification image, (c) medium magnification image, (d) high magnification image. (e) XRD profile of the dried particles obtained. (f) Particle size distribution derived by analyzing the SAXS intensity (Figure S2). (g) Absorption spectrum of the diluted particle dispersion.

The ZrN–$SiO_2$ core-shell particles were synthesized using the obtained ZrN dispersions. The dark-blue solution transformed to a white hue as the reaction proceeded (Figure S4). During this process, the solution did not undergo gelation and precipitation. After each reaction, the particles were collected by centrifugation. **Figure 2** shows the photographs of the particles obtained at each reaction time. The color of particles changed from dark purple to gray-white as the amount of silica produced increased with the reaction time. Subsequently, the morphology of the synthesized particles was examined using scanning transmission electron microscopy (STEM). **Figure 3** shows the high-angle annular dark-field (HAADF) STEM images of the particles obtained at various reaction times (40, 180, 300, and 1440 min). Spherical particles with internal cores are observed at all reaction times. The morphology of the core particles reflects the agglomeration state of the ZrN nanoparticles. Since ZrN particles are not present in a completely separated state of crystallites, as shown in **Figure 1(b)**, there are instances where agglomerated ZrN particles are coated with $SiO_2$. The particle sizes obtained at reaction times ranging from 40 to 1440 min are approximately 250 to 700 nm (Figure S5). As shown in **Figure 4**, the particle size distribution was obtained using the HAADF STEM images (Figure S6). The averages of the particle sizes are 289, 497, 628, and 715 nm at reaction times of 40, 180, 300, and 1440 min, respectively. Therefore, particles can be prepared by tuning the particle size and adjusting the shell thickness by varying the reaction time. Moreover, the HAADF STEM images are obtained by detecting forward-scattered electrons, and the intensity of these images is directly proportional to the atomic number of elements. Therefore, heavy atoms appear brighter, whereas light atoms appear darker. Interestingly, the HAADF STEM images revealed that the core area of the particle was brighter than the shell area, indicating a different composition between the core and shell.

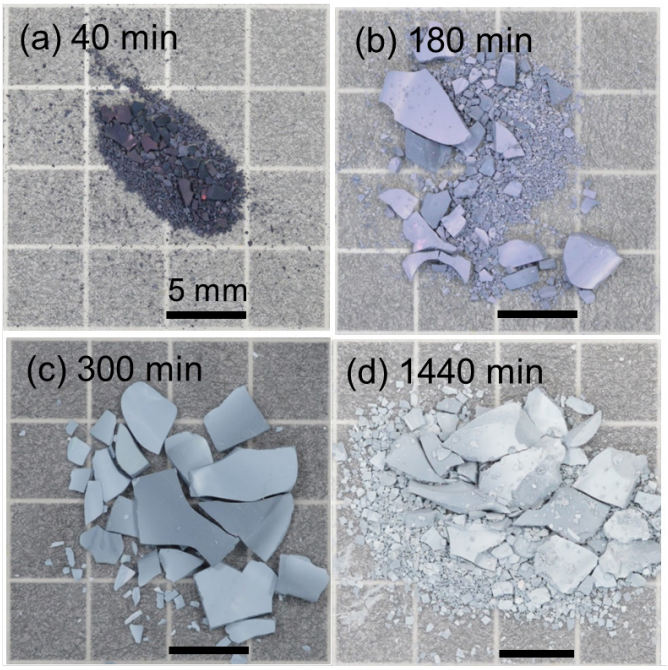


**Figure 2.** Photographs of particles synthesized at reaction times of (a) 40 min, (b) 180 min, (c) 300 min, and (d) 1440 min.

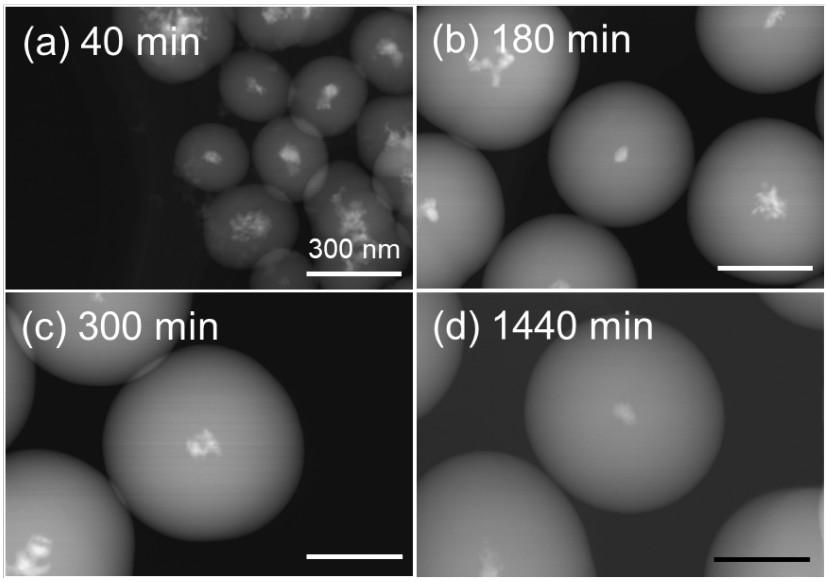


**Figure 3.** HAADF STEM images of the particles produced at the reaction times of (a) 40 min, (b) 180 min, (c) 300 min, and (d) 1440 min.

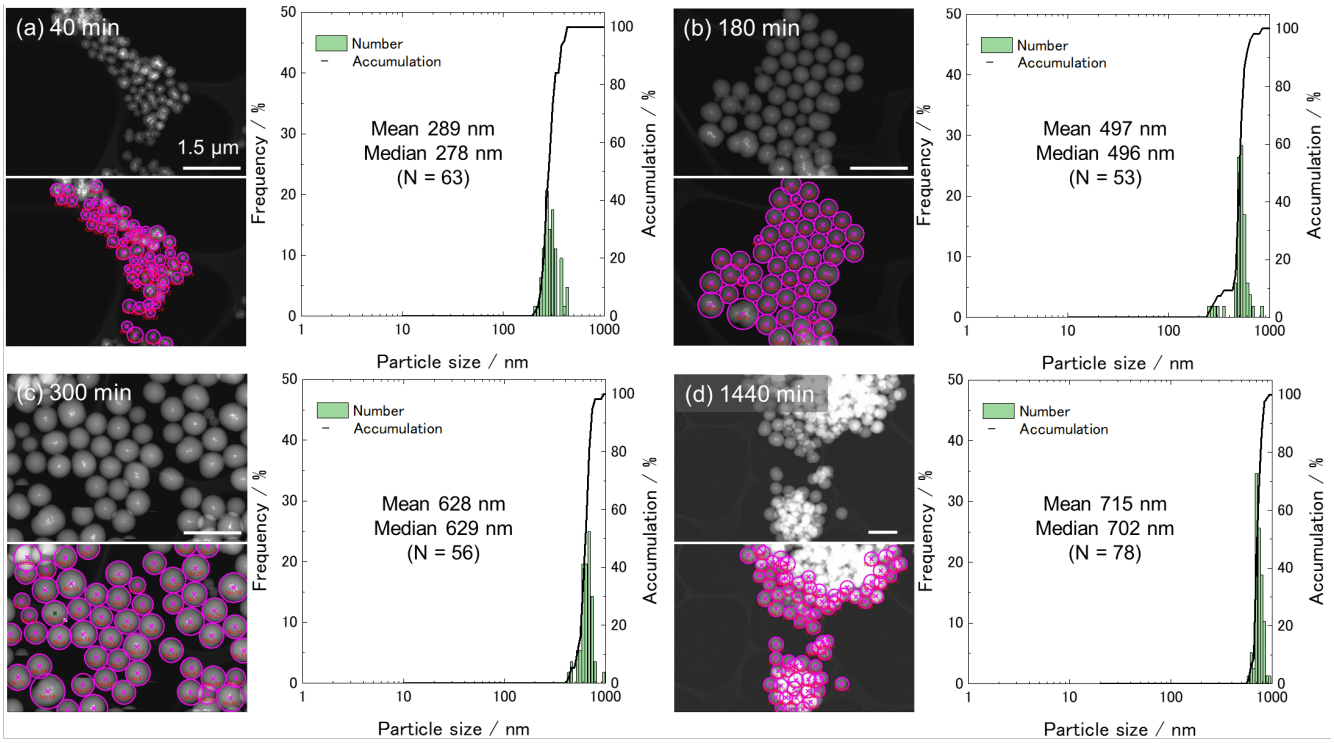


**Figure 4.** Size of the particles produced at the reaction times of (a) 40 min, (b) 180 min, (c) 300 min, and (d) 1440 min.

To investigate the shell formation FTIR and Raman spectra of the products at designated reaction times were measured (**Figure 5** and Figure S7). The FTIR spectra at reaction times of 0 min, 40 min, 180 min, 300 min, and 1440 min with the 4000–1500 $cm^{-1}$ range are displayed in **Figure 5(a)** and with the 1500–500 $cm^{-1}$ range in **Figure 5(b)**. **Figure 5(c)** presents the Raman spectra of the products. From FTIR and Raman spectra, the formation of $SiO_2$ was confirmed after 40 min, and the intensity of bands based on Si-O gradually increased with an increase in the reaction time. The intensity of the bands based on O-H groups decreased with an increase in the reaction time. These behaviors indicate that the $SiO_2$ network was formed with an increase in reaction time, and consistent with the trends observed in **Figures 3** and **4**. In addition, only very weak C-H bands based on unreacted ethoxy groups (around 3000 $cm^{-1}$) were observed. Because the intensity of the bands based on O-H groups and C-H groups in core–shell particles is very weak, we believe that the effect of the unreacted ethoxy group or O-H groups on the fabrication of particle assemblies is negligible.

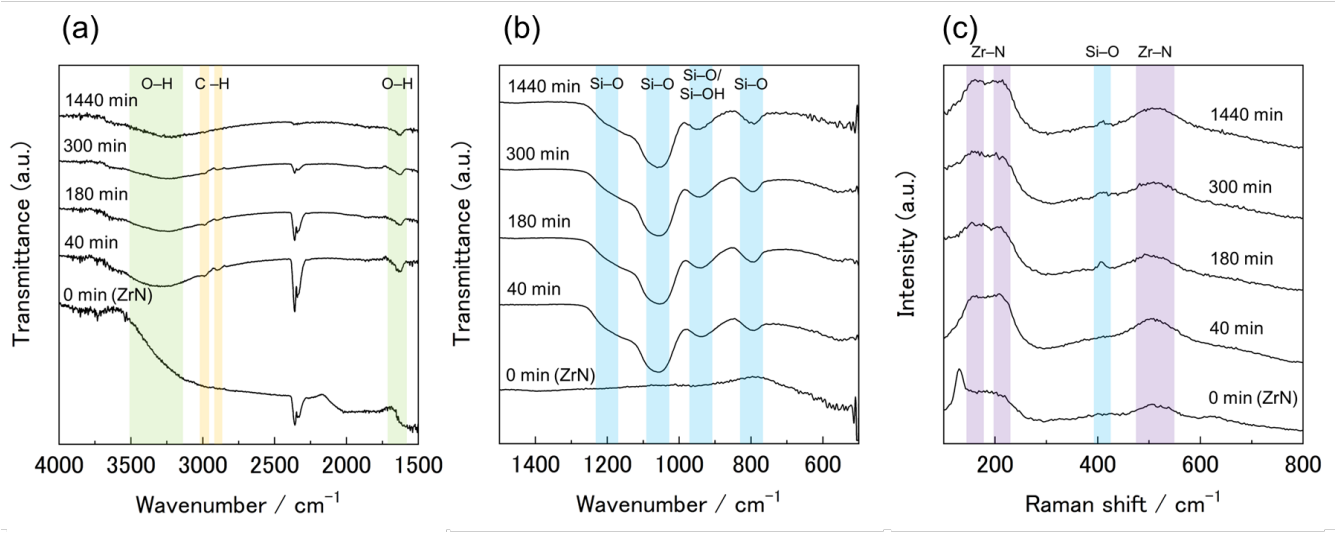


**Figure 5.** FTIR spectra of the particles produced at the reaction times of 0 min, 40 min, 180 min, 300 min, and 1440 min: (a) the 4000–1500 $cm^{-1}$ range and (b) the 1500–500 $cm^{-1}$ range. Absorption at approximately 2300 $cm^{-1}$, attributed to atmospheric $CO_2$, was detected in all samples. (c) Raman spectra of the produced particles.

Energy-dispersive X-ray spectroscopy (EDS) was employed to determine the elemental composition more precisely across different areas of the particles. From **Figure 6(a, b)**, the EDS line scan demonstrates a concentration of Zr predominantly in the core area and a concentration of Si in the shell region. This distinct elemental distribution suggests a core–shell structure, a conclusion further supported by TEM imaging, as displayed in **Figure 6(c)**. The TEM images showed specific features consistent with a core-shell morphology. The electron diffraction patterns in **Figure 6(d)** displayed distinct spots, indicating crystallinity within the particles. To further validate these findings and explore the specific phases present, XRD was conducted on the synthesized particles. XRD measurements, as illustrated in **Figure 6(e)**, revealed the presence of the ZrN phase in particles synthesized after a reaction time of 1440 minutes. Collating the data from STEM-EDS and XRD, it can be concluded that the particles synthesized possess a ZrN core and an $SiO_2$ shell, designating them as ZrN–$SiO_2$ core–shell particles. The resonance wavelength of particles exhibiting localized surface plasmon resonance is known to shift to longer wavelengths as the particle size increases. However, in the process of preparing core–shell particles in the

present study, the change in the size of the ZrN particles themselves that exhibit LSPR was not observed. Therefore, we believe that there is no need to consider changes in the absorption wavelength due to changes in ZrN particle size. The absorption wavelength of ZrN nanoparticles due to LSPR is presumed to shift towards longer wavelengths when surrounded by $SiO_2$, compared to when dispersed in water. This shift is attributed to the dependence of the LSPR resonance wavelength on the dielectric constant of the surrounding medium. The relative permittivity of water is approximately 1.33, while that of $SiO_2$ is approximately 3.9. A higher dielectric constant tends to elongate the LSPR resonance wavelength of nanoparticles, as it more strongly suppresses the oscillations of electrons around the particle, resulting in resonance at lower energy (longer wavelength).[42] Analyzing the LSPR effects in the submicron-sized core–shell particles fabricated in this study is challenging due to the dominant influence of overall particle scattering over absorption by the core's localized surface plasmon resonance. However, as observed in the obtained images (**Figure 2**), specific wavelength absorption leading to a purple coloration of the particles is confirmed for shell thicknesses up to 250 nm.

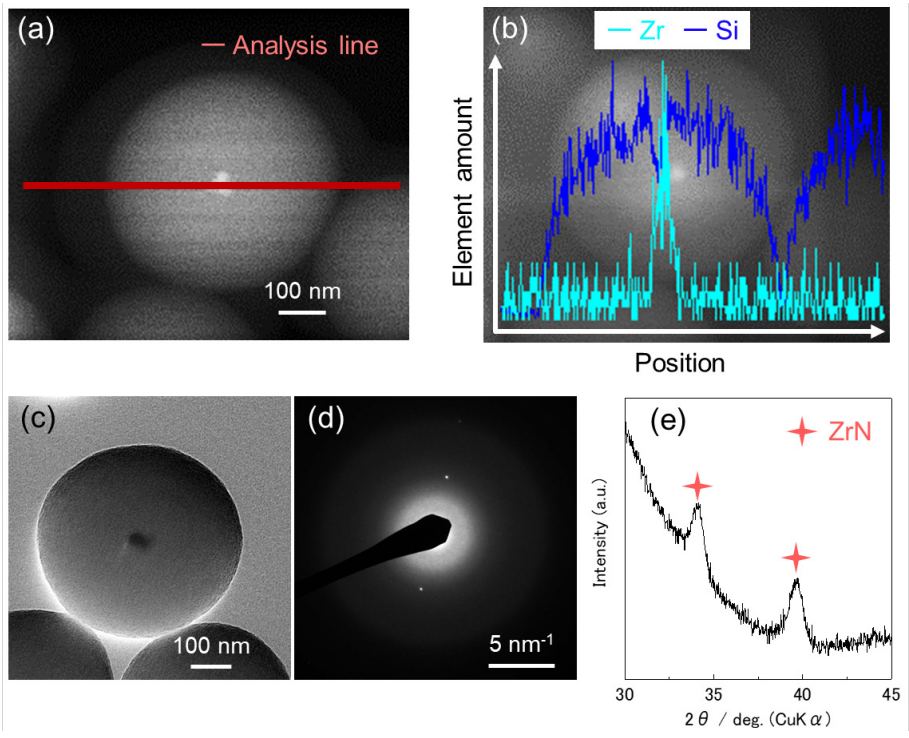


**Figure 6.** (a) HAADF STEM image of products with highlighted EDS analysis line. (b) Composition amount of the line across the particle. (c) TEM image of products. (d) Electron diffraction image of products. (e) XRD profile of the products.

The obtained ZrN–$SiO_2$ core–shell particles were stacked on a glass substrate by the layer-by-layer method using a poly(diallyl dimethylammonium chloride) (PDDA) solution. The layers of particles were formed on the surface of the substrate. Particle-stacked films comprising ZrN–$SiO_2$ core–shell particles were obtained (Figure S8). The thickness of the particle-stacked film was approximately 2 μm (Figure S9). The optical characteristics of the particle-stacked films of the obtained particles were assessed using reflection spectra.

**Figure 7** shows the reflection spectra of the particle-stacked films. In the case of the particle-stacked films containing ZrN–$SiO_2$ core–shell particles with diameters of 497, 628, and 715 nm, peaks appear at 542, 605, and 673 nm in the reflection spectra, respectively, as shown in **Figures 7(a, b)**. The particle-stacked film composed of ZrN–$SiO_2$ core–shell particles with particle size 289 nm did not exhibit a clear peak. In every instance, a peak was observed at approximately 330 nm. A similar peak at this wavelength was also evident in the $SiO_2$ substrate alone. This consistent occurrence suggests that the origin of the peak can be attributed to the intrinsic properties of the $SiO_2$ substrate. **Table 1** shows the summary of particle size, coefficient of variation (CV) which means monodispersity, and peak positions of particle-staked film. The coefficient of variation (CV) serves as a statistical metric to assess the homogeneity of particle size distributions. This is the standard deviation of the particle size distribution divided by the average particle diameter, and the lower the CV, the more uniform the particle size distribution. Conversely, a high CV indicates a large variation in particle size. In the reflection spectra derived from films stacked with particles, the observed maxima shift based on particle size (Figure S10). This shift suggests that these maxima indicate structural colors, arising from the strong reflection of specific wavelengths by periodic structures (i.e., Brag diffraction). However, the intensity is less than 10%, and the peaks are broad with large half-widths. The reason why the peaks with large half-widths in the case of 497, 628, and 715 nm, and no obvious peak in the case of 289 nm appear is due to the low monodispersity of the particles. The coefficient of variation is in the range of 8 to 18 % in the case of the particle obtained by this method. This result means that some kind of the obtained particles have sufficient

monodispersity to exhibit a structural color but are insufficient to develop a clear color as a structural color material. However, it is of significance that we were able to demonstrate ZrN–$SiO_2$ core-shell particle show structural color. The ZrN–$SiO_2$ core–shell particles have the potential to be the materials tuning the absorption and reflection spectra by the combination of LSPR and the periodic structure of components. Controlling absorption and reflection in narrower wavelength ranges requires more precise reaction control and improved particle monodispersity. More understanding of the reaction mechanism and adding ingredients such as surfactants to control the reaction should help achieve the ideal properties to tune the optical properties. We believe that ZrN–$SiO_2$ core–shell particles obtained by coating with $SiO_2$ via a liquid phase process can be a significant material for optical applications.

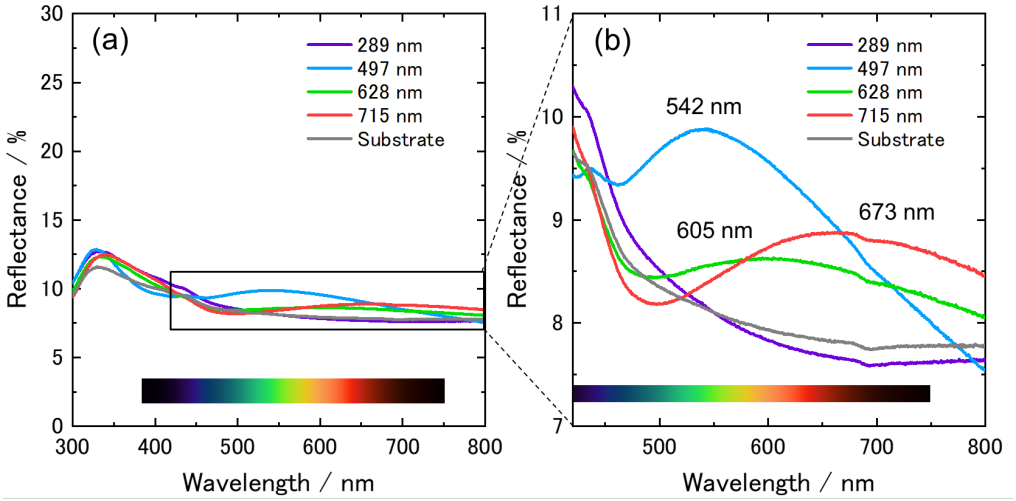


**Figure 7.** Reflection spectra of the particle-stacked films composed of ZrN–$SiO_2$ core-shell particles (a) with diameters of 289, 497, 628, and 715 nm, and its enlarged view (b).

**Table 1.** Summary of particle sizes (average±standard deviation), coefficient of variation (CV), and peak positions of particle-stacked films.

| Reaction time | Particle size / nm | CV / % | Peak position / nm |
|---|---|---|---|
| 40 min | 289±49 | 17 | - |
| 180 min | 497±91 | 18 | 542 |
| 300 min | 628±84 | 13 | 605 |
| 1440 min | 715±60 | 8 | 673 |

## CONCLUSIONS

We successfully coated a $SiO_2$ layer through a sol-gel process on the ZrN nanoparticles to form ZrN–$SiO_2$ core-shell particles. An increase in the $SiO_2$ shell thickness was achieved by increasing the reaction time, enabling a shift in the structural color reflection toward a long wavelength in the range of 500–700 nm. We believe that the liquid-phase process is applicable to coatings with other nitrides exhibiting plasmon resonance, and offers color tuning by LSPR and controllable periodic structures. ZrN–$SiO_2$ core–shell particles whose $SiO_2$ shell thickness is controllable can be a significant material for optical application.

## METHODS

### Materials

Zirconium dioxide ($ZrO_2$, 10 nm) was purchased from ITEC Co., Ltd. Magnesium nitride ($Mg_3N_2$) was purchased from Sigma Aldrich. Tetraethoxysilane (TEOS) was purchased from Fluorochem Ltd. Ammonia solution (30 wt. %) was purchased from KANTO CHEMICAL CO., INC. A poly (diallyl dimethylammonium chloride) (PDDA) solution (20 wt. % in $H_2O$) was purchased from Sigma-Aldrich. Hydrochloric acid (1 M) was purchased from KANTO CHEMICAL Co., Inc.

### Sample preparation

ZrN nanoparticle dispersion

ZrN nanoparticles were synthesized using a modified version of the process described by Karaballi et al.[22] A mixture of 1 g of zirconium dioxide nanopowder and a 3 molar excess of $Mg_3N_2$

powder was mixed using an agate mortar for 5 min in an Ar glove box. The resulting mixture was transferred to an alumina combustion boat and hermetically sealed in a plastic bag with a zip. The powder confined in the plastic bag was immediately inserted into a quartz tube and heated at 1000 °C for 12 h under nitrogen gas flow in a tubular furnace. After natural cooling to room temperature, 0.2 g of the final product was transferred to a beaker and mixed with 25 mL of 1.0 M HCl solution. The mixture was sonicated for 20 min and 20 mL of water was added. After stirring for 1 h, the supernatant was separated by centrifugation for 1 h at 11000 rpm. The residual precipitate was then redispersed in 5 mL of water by sonication and centrifuged for 15 min at 3300 rpm. The blue-colored supernatant was collected, and the precipitates were suspended in 5 mL of water by sonication. Finally, supernatants were collected. The ZrN concentration in the obtained dispersion was 0.03 wt%.

ZrN–$SiO_2$ core–shell nanoparticles

The ZrN nanoparticles were surface-coated with amorphous silica shells using a sol–gel process. A dispersion of ZrN nanoparticles (0.03 wt%, 2 mL) was mixed with 10 mL of ethanol. Under continuous stirring, 0.3 mL of ammonia solution was added dropwise to the mixture. Subsequently, TEOS (0.1 mL) was added to the reaction mixture every 20 min until the final volume reached 1 mL. The reaction was allowed to proceed for 40–1440 min at room temperature with continuous stirring. The resulting particles were separated from the reaction medium by centrifugation at 3000 rpm for 15 min and resuspended in water.

Particle-stacked films

The obtained ZrN–$SiO_2$ core–shell particles were arrayed on a glass substrate using a layer-by-layer technique. The glass slides were submerged in a 1 wt% PDDA solution for 10 min, washed thoroughly by immersing them in water for 10 min, and dried using $N_2$ gas. The dried glass plates were then dipped into a 1 wt% suspension of ZrN–$SiO_2$ core–shell particles for 10 min. The plates were washed by immersing them in water again for 10 min and dried using $N_2$ gas. The immersion and emersion of the plates in the solution, dispersion, or water were conducted manually, without the use of any specialized equipment. This process was repeated five times to produce films comprising five layers of ZrN–$SiO_2$ core-shell particles.

**Material Characterization**

X-ray Diffraction (XRD)

The crystalline phase was analyzed using an X-ray diffraction (XRD) diffractometer (Cu Ka, Mini-Flex 600, Rigaku, Japan). The diffraction angle 2θ was scanned in the range of 30 to 60° at a rate of 5°/min. XRD profiles of the core-shell nanoparticles were acquired at a scanning rate of 1°/min to mitigate the impact of noise.

Transmission Electron Microscopy (TEM)

The morphologies of the ZrN nanoparticles and core-shell nanoparticles were evaluated using TEM (JEM-2010, JEOL, Japan). The dispersions of ZrN nanoparticles and core-shell nanoparticles were drop-cast onto copper-mesh TEM grids. The acceleration voltage of the electron gun used for the observation was 200 kV.

Scanning Transmission Electron Microscopy (STEM)

The morphology of the core-shell particles was examined using scanning transmission electron microscopy (STEM) with an HD-2000 instrument (HITACHI, Japan). The sample was prepared following the same procedure as for the TEM observation, and the electron gun acceleration voltage was set at 200 kV. Energy-dispersive X-ray spectroscopy (EDS) was performed using the same equipment to investigate elemental distributions of the particles.

Small Angle X-ray Scattering (SAXS)

The particle size distribution of the ZrN nanoparticles in the dispersion was analyzed by small-angle X-ray scattering (SAXS) using high-intensity X-ray-generating equipment (SmartLab; Rigaku, Japan). The incident X-rays had a wavelength of 1.54 Å. The ZrN dispersion was loaded into capillaries with diameter of 2.0 mm and exposed to X-rays. The scattered X-rays within the range of 0–2° were detected, and the SAXS profiles were obtained to determine the particle size distribution.

UV-Vis absorption spectra measurement

The UV-Vis absorption spectra of the ZrN nanoparticle dispersions were recorded using a V-700 spectrometer (JASCO, Japan). For these measurements, the obtained ZrN nanoparticle dispersion was diluted tenfold with water. The diluted dispersion was then placed in a 1 cm square quartz cell and mounted on a holder for measurement. Water was used as the background for

absorbance measurements. The scanning rate was set at 200 nm $min^{-1}$ and the bandwidth was 2 nm, with a range of wavelengths scanned from 300 nm to 800 nm. The reflection spectra of the particle-stacked films were measured using the same instrument, equipped with an integrating spherical unit. The particle-stacked films were placed on a holder for measurement, and the scanning rate was set at 200 nm $min^{-1}$, with a bandwidth of 5 nm and a range of wavelengths scanned from 300 nm to 800 nm. The incident light is illuminated at an angle of 5° from the vertical plane of the sample.

FTIR absorption spectra measurement

The FTIR absorption spectra of the ZrN nanoparticle and ZrN–$SiO_2$ core–shell particles were measured using an FT/IR-4700 (JASCO, Japan) equipped with an Attenuated Total Reflectance (ATR) accessory. Spectra were collected in the range of 4000 to 500 $cm^{-1}$ with a resolution of 4 $cm^{-1}$, and each spectrum was obtained by averaging 32 scans to improve the signal-to-noise ratio. The samples were applied directly to the ATR crystal and gently pressed to ensure good contact. A background spectrum was recorded using a clean ATR crystal and was automatically subtracted from the sample spectra.

Raman spectra measurement

The Raman spectra of the samples were recorded using a Horiba XploRA Raman microscope (Horiba, Japan) equipped with a 532 nm laser. An attenuator filter was used to reduce the laser power to 0.1% at the sample to avoid sample damage. The spectra were collected in the range of

100 to 2600 $cm^{-1}$ with a spectral resolution of 1 $cm^{-1}$. Each spectrum was obtained by accumulating 10 scans with an exposure time of 150 seconds per scan. The samples were placed on a glass slide and examined under a 100x objective lens.

## ASSOCIATED CONTENT

### Supporting Information

The following files are available free of charge.

(1) STEM image of the starting material $ZrO_2$ nanoparticles; (2) XRD profiles of the products before washing; (3) SAXS profile of the obtained ZrN particle dispersion; (4) Photographs of the solution; (5) Low magnification HAADF STEM images of the ZrN–$SiO_2$ core-shell particles; (6) HAADF STEM images and target areas for analysis of the ZrN–$SiO_2$ core-shell particles; (7) FTIR spectra and Raman spectra of the produced particles; (8) Photographs of the particle-stacked film consisting of ZrN–$SiO_2$ core-shell particles; (9) Surface SEM image and cross-sectional SEM image of the prepared particle-stacked film; and (10) Reflection spectra normalized at the wavelength range 500–800 nm of the particle-stacked films. The authors have cited additional references within the Supporting Information.[43–45] (PDF)

## AUTHOR INFORMATION


### Corresponding Author

Kiyoharu Tadanaga

[2]Faculty of Engineering, Hokkaido University, Kita-13, Nishi-8, Kita-ku, Sapporo 060-8628, Japan; ORCID: https://orcid.org/0000-0002-3319-4353; Email: tadanaga@eng.hokudai.ac.jp

### Author

Shinji Noguchi

[1]Graduate School of Chemical Sciences and Engineering, Hokkaido University, Kita-13, Nishi-8, Kita-ku, Sapporo 060-8628, Japan; ORCID: https://orcid.org/0000-0003-1546-9998; Email: shinji@eis.hokudai.ac.jp

Akira Miura

[2]Faculty of Engineering, Hokkaido University, Kita-13, Nishi-8, Kita-ku, Sapporo 060-8628, Japan; ORCID: https://orcid.org/0000-0003-0388-9696; Email: amiura@eng.hokudai.ac.jp

## Author Contributions

- Shinji Noguchi led the study, including conceiving the study idea, developing the experimental plan, conducting the experiments, drafting the original manuscript, and securing a portion of the research funding.
- Akira Miura discussed the results.
- Kiyoharu Tadanaga played a multifaceted role, including conceiving the study idea, developing the experimental plan, securing a portion of the research funding, and overseeing the entire study's execution.

All authors reviewed the manuscript draft and revised it critically on intellectual content. All authors approved the final version of the manuscript to be published.

**Funding Source**

- Hokkaido University through Program for Leading Graduate Schools (Hokkaido University "Ambitious Leader's Program") from the Ministry of Education, Culture, Sports, Science and Technology (MEXT), Japan
- JST SPRING (Grant Number JPMJSP2119) from the Japan Science and Technology and Agency (JST)
- Grant-in-Aid for JSPS Fellows (No. 23KJ0014) from the Japan Society for the Promotion of Science (JSPS)
- Advanced Research Infrastructure for Materials and Nanotechnology in Japan (ARIM) of the MEXT. Grant Number JPMXP1223HK0087 (Hokkaido University).

**Notes**

The authors declare no competing financial interests.

**ACKNOWLEDGMENT**

Shinji Noguchi was supported by Hokkaido University through Program for Leading Graduate Schools (Hokkaido University "Ambitious Leader's Program") from the Ministry of Education, Culture, Sports, Science and Technology (MEXT), Japan. This research was financially supported by JST SPRING (Grant Number JPMJSP2119) from the Japan Science and Technology and Agency (JST) and a Grant-in-Aid for JSPS Fellows (No. 23KJ0014) from the Japan Society for the Promotion of Science (JSPS). We thank the open facility at Hokkaido University Sousei Hall for the use of SAXS, TEM, and STEM. This work was supported by "Advanced Research Infrastructure for Materials and Nanotechnology in Japan (ARIM)" of the MEXT. Grant Number JPMXP1223HK0087 (Hokkaido University). Shinji Noguchi is grateful to Dr. Tomokazu Yoshizawa, Dr. Yongming Wang, Dr. Yuko Mori, Dr. Naomi Hirai, Dr. Satoru Kimura, and Dr. Daisuke Yazaki of Hokkaido University for their helpful support in the use of SAXS, TEM, STEM, FTIR spectrophotometer, and Raman microscope.

## REFERENCES


1. Kim Y, Han Wi D, Wook Hong J, Woo Han S. Plasmonic Nanocrystal Assembly–Semiconductor Hybrids for Boosting Visible to Near-Infrared Photocatalysis. *ACS Nano*. 2023;17(18):18641–18651. https://doi.org/10.1021/acsnano.3c08182

2. Fan Y, Girard A, Waals M, Salzemann C, Courty A. Ag@Pt Core–Shell Nanoparticles for Plasmonic Catalysis. *ACS Appl Nano Mater*. 2023;6(2):1193–1202. https://doi.org/10.1021/acsanm.2c04767

3. Su H, Tian Q, Hurd Price CA, Xu L, Qian K, Liu J. Nanoporous core@shell particles: Design, preparation, applications in bioadsorption and biocatalysis. *Nano Today*. 2020;31:100834. https://doi.org/10.1016/J.NANTOD.2019.100834

4. Lou D, Zhu Z, Xu YF, *et al.* A core-shell catalyst design boosts the performance of photothermal reverse water gas shift catalysis. *Sci China Mater*. 2021;64(9):2212–2220. https://doi.org/10.1007/s40843-020-1630-2

5. Sahiner N, Butun S, Ilgin P. Hydrogel particles with core shell morphology for versatile applications: Environmental, biomedical and catalysis. *Colloids Surf A Physicochem Eng Asp*. 2011;386(1–3):16–24. https://doi.org/10.1016/J.COLSURFA.2011.06.023

6. Bayles A, Tian S, Zhou J, *et al.* Al@TiO2 Core–Shell Nanoparticles for Plasmonic Photocatalysis. *ACS Nano*. 2022;16(4):5839–5850. https://doi.org/10.1021/acsnano.1c10995

7. Han J, C. Freyman M, Feigenbaum E, Yong-Jin Han T. Electro-Optical Device with Tunable Transparency Using Colloidal Core/Shell Nanoparticles. *ACS Photonics*. 2018;5(4):1343–1350. https://doi.org/10.1021/acsphotonics.7b01337

8. Miranti R, Shin D, Dwi Septianto R, *et al.* Exclusive Electron Transport in Core@Shell PbTe@PbS Colloidal Semiconductor Nanocrystal Assemblies. *ACS Nano*. 2020;14(3):3242–3250. https://doi.org/10.1021/acsnano.9b08687

9. Li CL, Chang CJ, Chen JK. Fabrication of sandwich structured devices encapsulating core/shell SiO2/Fe3O4 nanoparticle microspheres as media for magneto-responsive transmittance. *Sens Actuators B Chem*. 2015;210:46–55. https://doi.org/10.1016/J.SNB.2014.12.094

10. S. Levin C, Hofmann C, A. Ali T, *et al.* Magnetic−Plasmonic Core−Shell Nanoparticles. *ACS Nano*. 2009;3(6):1379–1388. https://doi.org/10.1021/nn900118a

11. Yao K, Liu Y. Infrared Plasmonic Resonators Based on Self-Assembled Core–Shell Particles. *ACS Photonics*. 2017;5(3):844–851. https://doi.org/10.1021/acsphotonics.7b01012

12. Wei M, Serpe MJ. Temperature–Light Dual-Responsive Au@PNIPAm Core-Shell Microgel-Based Optical Devices. *Particle and Particle Systems Characterization*. 2019;36(1). https://doi.org/10.1002/ppsc.201800326

13. Palanikumar L, Kalmouni M, Houhou T, *et al.* pH-Responsive Upconversion Mesoporous Silica Nanospheres for Combined Multimodal Diagnostic Imaging and Targeted Photodynamic and Photothermal Cancer Therapy. *ACS Nano*. 2023;0(0). https://doi.org/10.1021/acsnano.3c04564

14. Garg A, Milina M, Ball M, *et al.* Transition-Metal Nitride Core@Noble-Metal Shell Nanoparticles as Highly CO Tolerant Catalysts. *Angewandte Chemie*. 2017;129(30):8954–8959. https://doi.org/10.1002/ange.201704632

15. Tian X, Tang H, Luo J, *et al.* High-Performance Core–Shell Catalyst with Nitride Nanoparticles as a Core: Well-Defined Titanium Copper Nitride Coated with an Atomic Pt Layer for the Oxygen Reduction Reaction. *ACS Catal*. 2017;7(6):3810–3817. https://doi.org/10.1021/acscatal.7b00366

16. Singh A, Shishodia MS. Graphene vs. silica coated refractory nitrides based core-shell nanoparticles for nanoplasmonic sensing. *Physica E Low Dimens Syst Nanostruct*. 2020;124:114288. https://doi.org/10.1016/J.PHYSE.2020.114288

17. Dong S, Chen X, Gu L, *et al.* TiN/VN composites with core/shell structure for supercapacitors. *Mater Res Bull*. 2011;46(6):835–839. https://doi.org/10.1016/J.MATERRESBULL.2011.02.028

18. Yang Y, Zeng R, Xiong Y, J. DiSalvo F, D. Abruña H. Cobalt-Based Nitride-Core Oxide-Shell Oxygen Reduction Electrocatalysts. *J Am Chem Soc*. 2019;141(49):19241–19245. https://doi.org/10.1021/jacs.9b10809

19. M. Tackett B, Sheng W, Kattel S, *et al.* Reducing Iridium Loading in Oxygen Evolution Reaction Electrocatalysts Using Core–Shell Particles with Nitride Cores. *ACS Catal*. 2018;8(3):2615–2621. https://doi.org/10.1021/acscatal.7b04410

20. Li Y, Yan Y, Ming H, Zheng J. One-step synthesis Fe3N surface-modified Fe3O4 nanoparticles with excellent lithium storage ability. *Appl Surf Sci*. 2014;305:683–688. https://doi.org/10.1016/J.APSUSC.2014.03.169

21. Kim H, Im PW, Piao Y. A Facile Route for the Preparation of Monodisperse Iron nitride at Silica Core/shell Nanostructures. *Front Bioeng Biotechnol*. 2021;9. https://doi.org/10.3389/fbioe.2021.735727

22. Karaballi RA, Humagain G, Fleischman BRA, *et al.* Synthesis of Plasmonic Group-4 Nitride Nanocrystals by Solid-State Metathesis. *Angewandte Chemie*. 2019;58:3–147. https://doi.org/10.1002/ange.201813134

23. Exarhos S, Alvarez-Barragan A, Aytan E, A. Balandin A, Mangolini L. Plasmonic Core–Shell Zirconium Nitride–Silicon Oxynitride Nanoparticles. *ACS Energy Lett*. 2018;3(10):2349–2356. https://doi.org/10.1021/acsenergylett.8b01478

24. Mohsen AA, Zahran M, Habib SED, Allam NK. Refractory plasmonics enabling 20% efficient lead-free perovskite solar cells. *Sci Rep*. 2020;10(1). https://doi.org/10.1038/s41598-020-63745-7

25. Noguchi S, Odahara J, Sakai H, Carolina Rosero-Navarro N, Miura A, Tadanaga K. Combustion Reactions between Transition-Metal Chlorides and Sodium Amide and Their Ignition Temperature. *Inorg Chem*. 2021;60(17):12753–12758. https://doi.org/10.1021/acs.inorgchem.1c00557

26. Miura A. Low-temperature synthesis and rational design of nitrides and oxynitrides for novel functional material development. *Journal of the Ceramic Society of Japan*. 2017;125(7):552–558.

27. Stöber W, Fink A, Bohn E. Controlled growth of monodisperse silica spheres in the micron size range. *J Colloid Interface Sci*. 1968;26(1):62–69. https://doi.org/10.1016/0021-9797(68)90272-5

28. Tadanaga K, Morita K, Mori K, Tatsumisago M. Synthesis of monodispersed silica nanoparticles with high concentration by the Stöber process. *J Solgel Sci Technol*. 2013;68(2):341–345. https://doi.org/10.1007/s10971-013-3175-6

29. Lee HB, Yoo YM, Han YH. Characteristic optical properties and synthesis of gold–silica core–shell colloids. *Scr Mater*. 2006;55(12):1127–1129. https://doi.org/10.1016/J.SCRIPTAMAT.2006.08.044

30. Ung T, Liz-Marzán LM, Mulvaney P. Gold nanoparticle thin films. *Colloids Surf A Physicochem Eng Asp*. 2002;202(2–3):119–126. https://doi.org/10.1016/S0927-7757(01)01083-4

31. Bahadur NM, Watanabe S, Furusawa T, *et al.* Rapid one-step synthesis, characterization and functionalization of silica coated gold nanoparticles. *Colloids Surf A Physicochem Eng Asp*. 2011;392(1):137–144. https://doi.org/10.1016/J.COLSURFA.2011.09.046

32. Engelbrekt C, Gargasya Y, Law M. Silica Shell Growth on Vitreophobic Gold Nanoparticles Probed by Plasmon Resonance Dynamics. *The Journal of Physical Chemistry C*. 2021;125(45):25119–25125. https://doi.org/10.1021/acs.jpcc.1c07969

33. Yang P, Ando M, Murase N. Various Au Nanoparticle Organizations Fabricated through SiO2 Monomer Induced Self-Assembly. *Langmuir*. 2011;27(3):895–901. https://doi.org/10.1021/la103143j

34. Luis Montaño-Priede J, Paulo Coelho J, Guerrero-Martínez A, Peña-Rodríguez O, Pal U. Fabrication of Monodispersed Au@SiO2 Nanoparticles with Highly Stable Silica Layers by Ultrasound-Assisted Stöber Method. *The Journal of Physical Chemistry C*. 2017;121(17):9543–9551. https://doi.org/10.1021/acs.jpcc.7b00933

35. Cathcart N, Murshid N, Campbell P, Kitaev V. Selective Plasmonic Sensing and Highly Ordered Metallodielectrics via Encapsulation of Plasmonic Metal Nanoparticles with Metal Oxides. *ACS Appl Nano Mater*. 2018;1(11):6514–6524. https://doi.org/10.1021/acsanm.8b01964

36. Han J, Lee E, Dudoff JK, *et al.* Tunable Amorphous Photonic Materials with Pigmentary Colloidal Nanostructures. *Adv Opt Mater*. 2017;5(7). https://doi.org/10.1002/adom.201600838

37. L. Ding H, X. Zhang Y, Wang S, M. Xu J, C. Xu S, H. Li G. Fe3O4@SiO2 Core/Shell Nanoparticles: The Silica Coating Regulations with a Single Core for Different Core Sizes and Shell Thicknesses. *Chemistry of Materials*. 2012;24(23):4572–4580. https://doi.org/10.1021/cm302828d

38. Zhong Q, Cao M, Hu H, *et al.* One-Pot Synthesis of Highly Stable CsPbBr3@SiO2 Core–Shell Nanoparticles. *ACS Nano*. 2018;12(8):8579–8587. https://doi.org/10.1021/acsnano.8b04209

39. Yang P, Ando M, Murase N. Highly Luminescent CdSe/CdxZn1–xS Quantum Dots Coated with Thickness-Controlled SiO2 Shell through Silanization. *Langmuir*. 2011;27(15):9535–9540. https://doi.org/10.1021/la201213c

40. J. Sandoval P, Lopez K, Arreola A, *et al.* Quantum Diamonds at the Beach: Chemical Insights into Silica Growth on Nanoscale Diamond using Multimodal Characterization and Simulation. *ACS Nanoscience Au*. 2023;0(0). https://doi.org/10.1021/acsnanoscienceau.3c00033

41. The Editors of Encyclopaedia Britannica. Rayleigh scattering. *Encyclopedia Britannica*. 2023.

42. Hong YA, Ha JW. Enhanced refractive index sensitivity of localized surface plasmon resonance inflection points in single hollow gold nanospheres with inner cavity. *Sci Rep*. 2022;12(1). https://doi.org/10.1038/s41598-022-11197-6

43. Chen XJ, Struzhkin V V., Kung S, Mao HK, Hemley RJ, Christensen AN. Pressure-induced phonon frequency shifts in transition-metal nitrides. *Phys Rev B Condens Matter Mater Phys*. 2004;70(1). https://doi.org/10.1103/PhysRevB.70.014501

44. Shah WH, Iqbal Y, Safeen A, *et al.* Study of the structural and electrical properties of silicon ion irradiated zirconium nitride thin films. *Modern Physics Letters B*. 2018;32(24):1850281. https://doi.org/10.1142/S0217984918502810

45. Sato Y, Hayami R, Gunji T. Characterization of NMR, IR, and Raman spectra for siloxanes and silsesquioxanes: a mini review. *J Solgel Sci Technol*. 2022;104(1):36–52. https://doi.org/10.1007/s10971-022-05920-y

Table of Contents (ToC)

